Additive Manufacturing 84 (2024) 104101

Contents lists available at ScienceDirect

Additive Manufacturing

journal homepage: www.elsevier.com/locate/addma

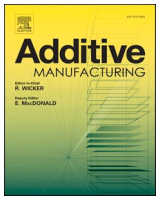

Flow mechanisms and their influence on the properties of EGaIn-graphene-poly(ethylene) oxide composites during material extrusion-based additive manufacturing

Ruchira Tandel [a], Irmak Sargin [b], B. Arda Gozen [a,*]

[a] Washington State University, School of Mechanical and Materials Engineering, United States
[b] Middle East Technical University, Department of Metallurgical and Materials Engineering, Ankara, Turkiye

ARTICLE INFO

Keywords:
Direct-ink writing
Shear flow
Wall slip
Rheology
Capillary rheometry

ABSTRACT

Polymer composites featuring room temperature liquid alloy particles complimenting other conductive fillers enable unique thermal and electrical properties. Direct-ink-writing approach is an intriguing processing path for these material systems, offering high resolution microstructural and property control. This paper investigates the composition-process-property relationships for material extrusion-based additive manufacturing of EGaIn-Graphene-Poly(ethylene) Oxide composites. Particularly, the influence of composite composition, printing nozzle size and flow rate on electrical conductivity is studied through a mechanistic approach. In that, capillary rheometry and flow modeling was performed to describe the contribution of shear flow and wall slip to the ink flow and how they drive the conductivity of printed structures for various composite ink compositions and process parameters. Influence of composition on material property and process driven conductivity were separately analyzed. Results indicate that EGaIn particles hinder material property-driven baseline average conductivity at high graphene loading. Shear flow and wall slip both increase conductivity. Graphene and total active material concentration increase wall slip and decrease shear flow, leading to a net negative effect of total active material concentration on conductivity. These findings will contribute to composite and process design towards additive manufacturing of composites with as-designed properties.

1. Introduction

Polymer composites exhibit unique bulk properties by synergistically combining the properties of filler particles (thermal and electrical conductivity) and polymer matrices (high modulus, toughness, elasticity). Due to these exceptional material properties, polymer composites are eminently used for applications such as soft robotics, energy storage devices, flexible electronics and tissue engineering. The functionality of parts and devices used for these applications is a strong function of the microstructure of the composites which is governed by their processing. Among the processing methods used for polymer composites, material extrusion-based additive manufacturing methods, particularly direct-ink-writing (DIW), has recently emerged as a favorable technique, due to its capability to direct filler morphology within each deposited micro-filament [1]. Processing-property relationships for DIW are governed by the complex ink flow mechanisms which are manifestations of ink rheology and ink-nozzle interactions such as wall-slip. As such, there is a need for fundamental research to understand these relationships towards realizing precise control over the properties of printed polymer composite structures.

Direct-Ink-Writing has been commonly applied to polymer composites featuring conductive solid-state micro and nano-fillers including carbonous ones such as carbon fibers [2,3], graphene flakes [4], graphite particles [5], and carbon nanotubes [6], and metallic ones such Ag, Cu [7,8]. Recently, particles of Gallium-based liquid metal (LM) alloys like Ga-In (commonly referred to eutectic GaIn or EGaIn), Ga-Sn have been considered as fillers in polymer composites. These spherical particles of diameters ranging from tens of nm to hundreds of microns can be created by ultrasonication of bulk liquid metals in various liquid media including solvents [9,10] and polymer solutions [11]. They exhibit a unique morphology at room temperature as they consist of a liquid core and solid shell of Ga_2O_3 for particles that are larger than 70 nanometer in diameter [12]. This unique nature renders these particles deformable unlike any other conductive fillers. This property has

* Corresponding author.
E-mail address: arda.gozen@wsu.edu (B.A. Gozen).

https://doi.org/10.1016/j.addma.2024.104101
Received 29 October 2023; Received in revised form 16 March 2024; Accepted 25 March 2024
Available online 2 April 2024
2214-8604/© 2024 Elsevier B.V. All rights reserved.

recently been shown to significantly influence the processing of the LM particle-based polymer composites, particularly DIW type additive manufacturing [13]. LM particles have also been used as secondary fillers in polymer composites, accompanying rigid fillers such as graphene [14], Ag [15], etc. In such systems, LM fillers can act as stretchable anchors ensuring conductivity under large strains [16] or improve the thermal [14,17] piezoelectric properties [18] of the composites. Our earlier work has shown that LM fillers significantly affected the rheology and processing of the complex precursors of such material systems [4,19]. Particularly in the case of direct-ink-writing using solvent-based inks including graphene as a rigid filler, it was shown that the introduction of EGaIn particles increases the ink viscoelasticity and improves the printability through DIW [4]. These results highlight the need for further studies on the composition-processing-property relationships pertaining to DIW of LM-based polymer composites, particularly how LMs can influence the microstructural evolution of polymer composites during DIW.

It is known that shear and extensional flows experienced by the composite inks inside the printing nozzles influence the morphology of the fillers, directly dictating the final microstructure and functional properties. Ink rheology is a critical factor determining the nature of such flows, yet, understanding ink rheology is not sufficient to fully and quantitatively understand the shear and extensional flows experienced by the inks during DIW. The other critical and often overlooked factor influencing ink flow is wall-slip, which is particularly prominent for polymer composite inks with high solid loading [20,21]. Increasing wall slip generally reduces the magnitude of shear strain rates that are responsible for filler alignment [2], hindering the capability of DIW to dictate the part microstructure. Despite this conventional understanding, in-depth study on how wall-slip affects the part microstructure evolution during DIW of polymer composites is missing. Furthermore, the influence of LM particles included in polymer composite inks on the wall slip during DIW is not clear, particularly given their deformable nature unlike solid fillers.

In this paper, towards addressing these gaps in the literature, we present an in-depth study of the compositional and process related factors that determine the electrical conductivity of the printed polymer composites consisting of EGaIn particles and graphene flakes in a Polyethylene Oxide binder. Particularly, the effect of ink composition, nozzle size and flow rate on printed parts electrical conductivity is investigated. In that, a mechanistic understanding is sought after thorough studying how these variables dictate key aspects of ink flow such as wall slip and shear deformation rate which are known to influence part microstructure and thus conductivity. This analysis has been performed through extensive capillary and rotational rheometry of various ink compositions. The rheological characterization data has been used to model of non-Newtonian capillary flow of inks through the nozzles incorporating non-linear wall slip effects. Finally, test structures were printed, and their electrical conductivity were characterized.

2. Materials and methods

2.1. Materials and ink preparation

Inks used in this study consist of a Polyethylene Oxide (PEO) blend as a binder, two types of conductive fillers; Graphene nano-powder (Grade: AO-4: 60 nm, purchased from Graphene Supermarket) and EGaIn micro particles (75% Gallium, 25% Indium by weight), in an Acetonitrile medium (anhydrous, 99.8%). The PEO blend consists of two different molecular weight PEO (LWM: 10^5 g/mol and HMW: 5×10^6 g/mol, purchased from Sigma Aldrich). Various ink compositions studied in this work are listed in Table 1.

Ink preparation starts with bulk EGaIn being broken into smaller segments in acetonitrile using a vortex mixer (Oxford BenchMate Mini Vortex Mixer) followed by ultrasonication (YUCHENGTECH Ultrasonic Homogenizer Sonicator Processor Mixer, 600 W, 20–500 ml) to form particles. Particles have an average size of 2.5 μm with a standard deviation of 1.2 μm evaluated among 500 particles imaged through SEM. The particle size distribution is given in supporting information Fig S1. LMW PEO and graphene were gradually added using a mechanical mixer (Cole-Parmer Compact Digital Mixer System) at the speed of 300 RPM. After 25 mins of continuous mixing, HMW PEO was gradually added at 150–200 RPM to avoid the rod climbing effect. This ink was continuously mixed for an additional 15−20 mins to obtain a homogenous paste and then was stored in 30cc syringes. Prior to experimentation, the inks were transferred to a 5cc steel syringe which was centrifuged at 4000 RPM (using a Nordson Processmate 5000 centrifuge) for 30–60 mins to evacuate the trapped air.

Table 1
Volumetric compositions and the names of the inks used. Values are given in % vol.

TERMS	EGaIn	Graphene	PEO	ACETONITRILE
E1.8G12.1P13.9	1.8	12.1	13.9	72.0
E2.9G11.6P14.4	2.9	11.6	14.4	71.1
E3.8G10.4P14.2	3.8	10.4	14.2	71.7
E5G10P15	5.0	10.0	15.0	70.0
E2.6G10.5P17.1	2.6	10.5	17.1	69.8
E0.5G10.8P17	0.5	10.8	17.0	71.7
E1.93G9.67P17.41	1.9	9.6	17.4	70.9
E2.9G8.7P17.5	2.9	8.7	17.5	70.9
E2G11.2P15.3	2.0	11.2	15.3	71.5
E0G12P15	0.0	12.0	15.0	74.0
E0G10.2P13.9	0.0	10.2	13.9	75.9

2.2. Characterization and modeling of shear flow and wall slip

2.2.1. Shear rheology

The shear rheology of these inks was characterized using a TA instrument Ares G2 strain-controlled rotational rheometer. A serrated parallel plate geometry with a diameter of 25 mm was used to conduct the experiments. A plate gap of 1 mm was utilized, and non-volatile mineral oil was applied at the outer rim plates to prevent solvent evaporation from the inks during the experiments. Prior to the experiments, the material samples were pre-sheared at a strain rate of $1e^{-3}$ s^{-1} to overcome the transient effects. A flow sweep experiment was performed for each ink composition, where the inks were subjected to stepwise changing strain rates in the range of 5×10^{-4} s^{-1} to 5×10^{-2} s^{-1} through continuous top plate rotation. The torque on the top plate was measured during this process to determine the rate dependent shear stress profile for each material. These tests were run in the decreasing strain rate direction to reduce the transient effects that are commonly observed at low strain rates.

2.2.2. Capillary rheometry

Capillary rheometry tests were performed for each ink composition using a custom-built hybrid DIW printhead with capillary rheometry capability similar to the several other example systems demonstrated in the literature [22]. A brief description of this system is provided in the supporting information section S1 and it is described in detail in our earlier work [23]. This system gives us the capability to prescribe an extrusion pressure and monitor the steady-state flow rate in real time.

In capillary rheometry experiments, nozzles having four different diameters (250, 300, 400 and 600 μm) with two different lengths (13 mm and 25.4 mm) were used. The nozzle design is such that the flow enters the nozzles through an abrupt diameter reduction from 1.8 mm to the specific nozzle diameter. These tests were conducted by extruding each material at four different flow rates for each nozzle corresponding to the apparent strain rates that are in the 9–125 s^{-1} range. Here, the apparent strain rate ($\dot{\gamma}_a$) is given by

$$\dot{Y}_a = \frac{4Q}{\pi R^3} \tag{1}$$

where Q is the ink flow rate and r is the radius of the nozzle. To produce the flow rate vs. pressure data for each material-nozzle combination, we first determined the extrusion pressure that yields a flow rate corresponding to the low end of the strain rate range. Next, three additional pressures were iteratively selected to ensure that approximately the same flow rates are tested for nozzles having the same diameter but different lengths, while staying within the system's allowable pressure range of 5–225 psi. As a result, the exact values of the apparent strain rate were marginally different for each ink composition.

The pressure vs. flow rate (P-Q) data obtained for each nozzle-ink composition were then fitted to a power-law function of the general form

$$P_{R,L} = K_{R,L} Q^{n_{R,L}} \tag{2}$$

where $K_{R,L}$ and $n_{R,L}$ are power-law parameters corresponding to the nozzle with radius R and length L. These equations were then utilized to perform the Bagley analysis to determine the true wall shear stress for each experiment. To this end, for a given ink, we determine the maximum and minimum flowrate measured for each nozzle radius across the two lengths. Six equidistant flowrate points were then calculated in this range. For each flowrate point, the apparent strain rate was calculated using Eq. 1. The corresponding pressures were calculated for two different lengths of the nozzle radius using Eq. 2. The actual wall shear stress for all the flow flowrate points were then calculated by linear regression between the pressures calculated for each nozzle length with respect to the length over radius ratio as follows.

$$P_{R,L} = 2\tau_{w,R}\left(\frac{L}{R}\right) + P_{ent,R} \tag{3}$$

where $\tau_{w,R}$ is the actual wall shear stress and $P_{ent,R}$ is the pressure loss at the nozzle entrance [24]. Next, the apparent strain rate vs. true wall stress data across the determined flow rates were fitted with a power law as

$$\dot{\gamma}_{a,R} = A_R {\tau_{w,R}}^{mR} \tag{4}$$

where A_R and m_R are power-law parameters.Pressure loss at the entry is assumed to be equal to the extensional stress experienced by the ink as it enters the narrow nozzle capillary [24].

2.2.3. Model Fitting

To elucidate the flow mechanisms, specifically the contribution of wall slip and shear to the overall ink flow for different ink compositions under various DIW process conditions, we utilize the rotational and capillary rheometry data to construct a process model. This model correlates the apparent strain rate observed during the ink flow to its two main contributors that are wall slip and shear flow [20,25]

$$\dot{\gamma}_a = \dot{\gamma}_a^{slip} + \dot{\gamma}_a^{shear} \tag{5}$$

Each of these terms are explicitly correlated to the shear stress at the wall and several material properties. Particularly, the slip portion can be approximated by the model form:

$$\dot{\gamma}_a^{slip} = \frac{4\beta\tau^m}{R^{x+1}} \tag{6}$$

where τ is the wall shear stress, β, m and x are constants representing the non-linear relationship between the wall slip and the shear stress [25]. The shear term is given by the general formula [20]:

$$\dot{\gamma}_a^{shear} = \frac{4}{\tau^3}\int_0^{\tau} \tau^4 \dot{\gamma}(\tau) d\tau \tag{7}$$

where $\dot{\gamma}$ is the true rate of shear experienced by the ink. For this term to be evaluated, the functional relationship between the shear stress and the strain rate of the material needs to be known. For most highly loaded inks, the Herschel-Bulkley material model is a good representation of this functional relationship [26]:

$$\dot{\gamma}(\tau) = \frac{(\tau - \tau_y)^{1/n}}{K} \tag{8}$$

where τ_y is the yield stress, K is the consistency factor and the n is the power-law. With this model integrated, the shear component of the apparent strain rate becomes,

$$\dot{\gamma}_a^{shear} = \frac{4\tau^{1/n}}{K^{1/n}}\left(\frac{\tau_y^2(1-\tau_y/\tau)^{1+1/n}}{\tau^2(1+1/n)} + \frac{2\tau_y(1-\tau_y/\tau)^{2+1/n}}{\tau(2+1/n)} + \frac{(1-\tau_y/\tau)^{3+1/n}}{(3+1/n)}\right) \tag{9}$$

To perform the model fitting, capillary rheometry data is fitted to Eqs. 5, 6 and 9, while simultaneously the rotational rheometry data is fitted to Eq. 8, by optimizing the constants β, m, x, K, n and τ_y. The capillary rheometry data for this fitting practice is populated using Eq. 4 for each composition- nozzle pair, within the tested wall stress range. The model fitting was performed as a bounded non-linear optimization using fmincon function of MATLAB which uses the interior-point algorithm [27]. Here each variable is bounded to be greater than 0 to ensure physicality and the n variable was bounded between 0 and 1 to ensure shear thinning nature. The initial guesses for each variable were varied to ensure that the final results did not significantly vary due to complications from local minima. Further details on the optimization approach used during model fitting are provided in the supporting information section S2.

This model is then used for each printing experiment to determine several key parameters elucidating the ink flow mechanisms pertaining to wall slip and shear. Particularly, the true shear strain rate the ink experiences at the nozzle wall is given by

$$\dot{\gamma}(R) = \frac{\tau^{1/n}}{K^{1/n}}(1-\tau_y/\tau)^{1/n} \tag{10}$$

Here, wall stress can be determined by initially estimating the pressure required to achieve the observed flow rates during the printing experiments but with the longer nozzles, using Eq. 2. This equation is then used along with the flow rate and pressure measured during the printing with a shorter nozzle to apply the Bagley correction. This process determines the true wall stress and entrance pressure loss (P_{ent}) using Eq. 3.

Here, the slip velocity is given by

$$v_s = \frac{\beta\tau^m}{R^x} \tag{11}$$

The percent contribution of wall slip and shear mechanisms to the total apparent strain rate are then given by:

$$Slip\% = \frac{\dot{\gamma}_a^{slip}}{\dot{\gamma}_a} \times 100, shear\% = \frac{\dot{\gamma}_a^{shear}}{\dot{\gamma}_a} \times 100 \tag{12}$$

Finally, the pressure loss at the nozzle entry was used to estimate the rate of extensional strain rate ink experiences using the Cogswell method [28] as follows:

$$\dot{\varepsilon} = \frac{4\tau\dot{\gamma}_a}{3(1+1/m_R)P_{ent}} \tag{13}$$

It should be noted that the Cogswell relation is a rough estimate for extensional strain rate for complex, viscoelastic fluids such the studied here. For a better estimate, flow pattern at the nozzle entrance needs to be understood [24]. Our system and our highly opaque inks unfortunately did not allow us to visually observe the entrance to deduce parameters such as the entrance angle exhibited by the inks. As such, we resorted to using the Cogswell equation, which is the main approach adopted by most commercial capillary rheometers.

2.3. Direct-ink-writing (DIW) experiments and print characterization

2.3.1. DIW experiment parameters

DIW experiments were conducted to study how different flow mechanisms influence the properties of the 3D printed composites. The custom-built hybrid DIW printhead was used to print lines at various flow rate levels for each ink composition. Steel nozzles with four different diameters of 250, 300, 400 and 600 μm were used with a constant length of 13 mm. Lines were printed on glass substrates with a standoff distance equal to the nozzle diameter. For each ink composition, three apparent strain rate levels were determined. These strain rates were calculated through Eq. 1, using the lowest, highest and the midpoint flowrates obtained from the capillary rheometry experiments corresponding to the 600 μm diameter nozzle. The flowrates for the other three nozzles were then calculated at these apparent strain rate levels using Eq. 1. An effort was made to keep these strain rate levels constant across nozzle diameters and ink compositions, but variations were observed due to experimental limitations. Accordingly, a generic notation for low (L), medium (M) and high (H) apparent strain rate cases were used in the rest of this paper. The exact strain rate values used during the DIW experiments are given in Table S1. Printing was performed using the constant pressure mode of the printhead that allows for rapid stabilization of the flow rate [23]. The *P*-*Q* relation data obtained in Sec. 2.1.3. was used to determine pressure levels required to print the ink at the predetermined flowrates for each nozzle.

The substrate was hosted on a 3-axis motion system (Aerotech ANT180-ANT130 stages) to generate the printing motions whereas the printhead was kept stationary. The printing speeds were selected to be equal to the average speed of the ink flow at the nozzle exit to ensure balanced extrusion:

$$f = \frac{Q}{\pi R^2} \tag{14}$$

where f is the printing speed, Q is the ink flow rate and R is the nozzle radius. Three lines were printed for each ink-nozzle-flow rate combination to study the repeatability. A microscope camera is incorporated to visualize the printing behavior during these experiments as shown in Fig. 1(a).

2.3.2. Optical characterization of the print geometry

To quantitatively characterize the geometry of the prints 3D profilometer (Zygo NewView 6300) with a 50x scan lens was used. Geometric features such as width, height and cross-sectional area were measured to be used in calculations of electrical conductivity detailed in Section 2.5. The cross-section of the printed lines are depicted in Fig. 1(b). As shown, the base width (a) is smaller than the overall width of the lines (b), preventing the profilometry from capturing the base-width measurement. To address this issue, base width was measured through optical microscopy (Zeiss Axion 105) images taken from the bottom of the glass slides as shown in the Fig. 1(b). The data obtained was further analyzed using a MATLAB program to get an approximated cross-sectional area (A_M) of the printed line.

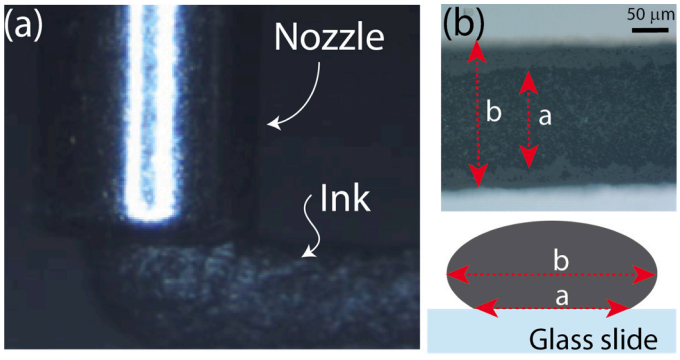

Fig. 1. (a) Microscope image of the DIW process, (b) Details of the cross-sectional area analysis.

To consider the porosity of the printed structure, we conducted various observations. First, the solid volume percentage (s) was calculated by weighing and subtracting the ink mass before and after evaporation, followed by dividing the result by the solid concentration. Subsequently, it was then utilized to calculate the expected cross-sectional area (A_p) of the printed structure after evaporation, which is given by

$$Ap = Q * f * s \tag{15}$$

Finally, the porosity of the printed structure was calculated by,

$$P = \frac{1 - Ap}{A_M} \tag{16}$$

2.3.3. Microstructural characterization (SEM) of the prints

Scanning Electron Microscope (SEM, FEI Quanta 200 F, ThermoFisher) with a 400–1000x zoom, 10–14 mm working distance and 10–20 kV beam power was used to scan the cross-sectional area of the printed lines to analyze the morphology of the constituents. SEM samples were prepared as follows: lines were printed on a scored glass substrate, which was subsequently broken after the printing process. This breakage allowed for a cross-sectional view of the printed lines, which was utilized for SEM analysis.

2.3.4. Measurement of printed line conductivity

The electric conductivity of the printed lines was characterized using the four-probe Kelvin method to measure the DC resistance across the line using an LCR meter (BK Precision Model 894, 500 kHz). On each line, EGaIn droplets were used as soft electrical contacts to establish robust connection to the printed lines, without damaging them as shown in Fig. 2(a-b). Resistance is measured among various lengths on the same line. To this end, the EGaIn droplets are placed on the lines using a syringe and a needle, starting from the pair that are farthest apart from each other, followed by another pair that is approximately 5 mm away from the first pair toward the center of the lines. These four contacts are then used to obtain the resistance measurement for the largest length such that the outer and inner pairs are used as the current and voltage contacts, respectively, in the four-point configuration. Next, another contact pair is added to the lines, approximately 5 mm away from the second pair, inward, to be used as the voltage contacts for the second largest length measurement. For each subsequent measurement, the voltage contacts for the previous measurement are used as the current contacts. A sample resistance vs length plot is provided in Fig. 2(c).

Obtained resistance measurements are further analyzed using the line transmission method [29] assuming the same cross-sectional area across the line length. Thereafter, the resistance is represented as a linear function of the line length;

$$R = \frac{1}{\sigma A} L + R_c \tag{17}$$

Where R is the resistance, σ is the conductivity of the line, A is the cross-sectional area of the line determined in Section 2.3.2, L is the length of the line, measured using image processing program (ZYGO), and R_c is the contact resistance. The slope of the *R*-*L* linear regression is used to calculate the conductivity of the printed line.

2.4. Analysis of the experimental data

To understand the influence of the key material and process parameters on the printed structure conductivity, we analyze the experimental data by considering three levels of variables as shown in Fig. 3.

We differentiated the experimental data into compositional parameters (EG, Gr, PEO and Act) where Act = EG +Gr + PEO is the total

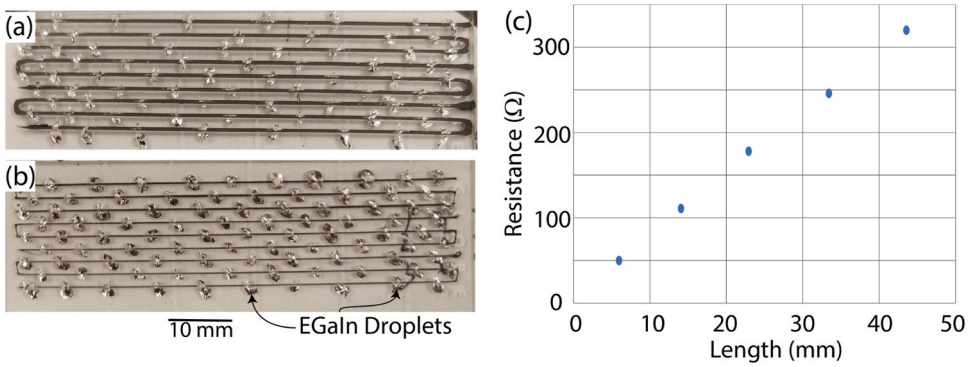

Fig. 2. (a-b) Representative images of the printed lines with soft liquid metal electrical contacts, printed using 600 (a) and 250 μm (b) diameter nozzles (c) Sample resistance vs length data for a printed ink.

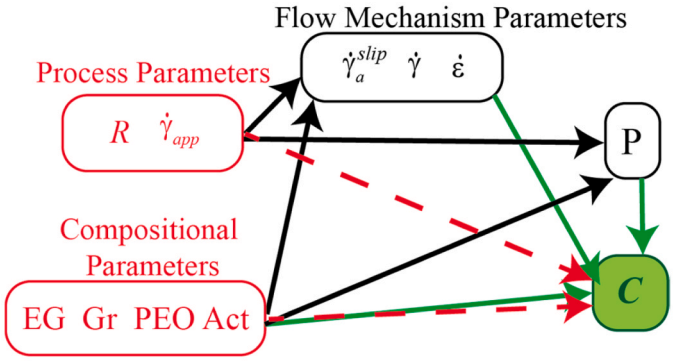

Fig. 3. Schematic description of the relationships between various parameters.

active material concentration, process parameters (R and $\dot{\gamma}_a$), flow mechanism parameters ($\dot{\gamma}_a^{slip}$, $\dot{\gamma}$ and $\dot{\varepsilon}$), porosity (P) and Conductivity (C). Here, the compositional and process parameters can be considered as process inputs and conductivity can be considered as the process output. Flow mechanism parameters and porosity can be considered as intermediate variables since they are dependent on the process inputs but also can have a direct influence on the conductivity. In fact, we postulate in this study that the intermediate parameters mechanistically explain how process parameters (R and $\dot{\gamma}_a$) dictate the printed line conductivity.

It is expected that the material composition will affect the conductivity and porosity through both inherent ways (e.g. generally one would expect increasing the concentration of conductive species will increase the inherent conductivity of the composite) and through processing mechanisms (e.g. increasing the concentration of a given constituent may increase wall slip or shear strain rate, affecting the microstructure of the conductive species thus the resultant conductivity). To capture the former effect, we calculated baseline average conductivity and porosity for each material by averaging these metrics across all printing experiments conducted for that material. Here average conductivity and porosity are given as $C^* = \frac{1}{12}\sum_{i=1}^{12} C_{ik}$ and $P^* = \frac{1}{12}\sum_{i=1}^{12} P_{ik}$, where C_{ik} and P_{ik} are the conductivity and porosity correspond to the experiment i (i.e. specific R-$\dot{\gamma}_a$ combination) for the composition k, respectively. These average quantities provide a measure of the baseline conductivity and porosity for each composition by removing the processing effects. To understand the isolated processing effects, we considered normalized conductivity and porosity given by $\overline{C} = C - C^*$ and $\overline{P} = P - P^*$.

To elucidate how the average and normalized conductivity is influenced by the input and intermediate variables, we employed several analysis techniques. First, stepwise linear regression was performed to obtain models representing the relationships highlighted in Fig. 3 between various variable types. These models are summarized below in Eq. 18.

$$\begin{aligned} C^* &\approx g^*(EG, Gr, PEO, Act, P^*) \\ P^* &\approx h^*(EG, Gr, PEO, Act) \\ \overline{C} &\approx f(R, \dot{\gamma}_a, EG, Gr, PEO, Act) \\ \overline{C} &\approx g\left(\dot{\gamma}_a^{slip}, \dot{\gamma}, P, EG, Gr, PEO, Act\right) \\ \overline{P}, \dot{\gamma}_a^{slip}, \dot{\gamma}, \dot{\varepsilon} &\approx h_i(R, \dot{\gamma}_a, EG, Gr, PEO, Act) \text{for i} = \overline{P}, \dot{\gamma}_a^{slip}, \dot{\gamma}, \dot{\varepsilon} \end{aligned} \tag{18}$$

In addition to this analysis, we also studied the relationship between the compositional parameters and the rheological parameters obtained through capillary and rotational rheometry, and model fitting as follows:

$$\left(\tau_y, n, K, \beta, m, x\right) \approx r_i(EG, Gr, PEO, Act) \text{for i} = \tau_y n, K, \beta, m, x \tag{19a}$$

Details of the stepwise regression process are provided in the supporting information section S3. In each of these models, only the listed input terms and their first order interactions were allowed. The stepwise regression identifies the statistically significant inputs and their interactions as terms in each of the models given in Eq.17. Next, we calculated several statistical quantities to understand the relative importance of these terms. In that, (i) we performed Analysis of Variance (ANOVA) on the data to obtain the Type 3 sum of squares value (SSQ) associated with each term that appears in the regression, (ii) we determined standardized regression coefficients (Coefficient) by multiplying the regression coefficient of each term with the variance of the term itself and dividing by the variance of the output, (iii) we calculated the partial correlations ($\rho_{partial}$) between each term and the output and (iv) an importance metric (Im) proposed by Hoffman[30] determined through multiplication of the quantities given in (ii) and (iii). Finally, we calculated the raw correlations (ρ_{raw}) for the linear terms to understand the sign of the net effect of the corresponding variable on the output.

3. Results and discussions

3.1. Capillary rheometry, model fitting and printing experiments

Raw pressure vs flow rate data corresponding to two ink compositions, E3.8G10.4P14.2 and E0G10.2P13.9, obtained using the short 250 μm and 600 μm diameter nozzles is shown in Fig. 4(a). In this plot, different colors represent different ink compositions, circle and triangle markers represent different nozzle lengths and the dashed lines are the power-law fits given with the corresponding coefficients of determination (R^2 values). R^2 values very close to 1 demonstrate that these fits that are used for the rest of the analysis, represent the experimental data with high accuracy. Since E0G10.2P13.9 replaces 3.8% EGaIn by volume with acetonitrile, it is expected to exhibit lower viscosity [19], leading it to flow at higher rates at the same pressure levels according to the shear flow theory. The results suggest that this is only true at low flow rates, as the curves converge at high flow rates. This behavior is associated with

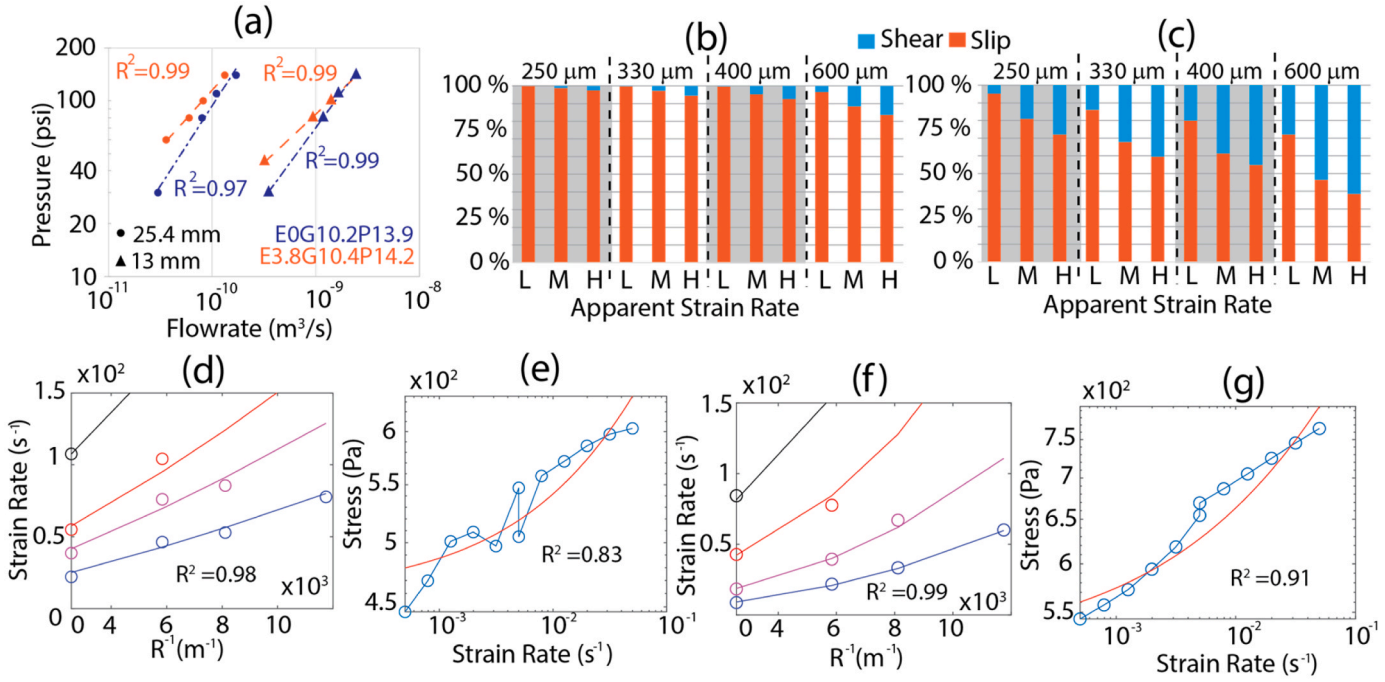

Fig. 4. (a) P-Q relations for E3.8G10.4P14.2 and E0G10.2P13.9, featuring nozzles with same radius and two different lengths. (b-c) Slip and Shear contributions to the apparent strain rate for inks E3.8G10.4P14.2 and E0G10.2P13.9, respectively. (d-e) Flow model fits for E3.8G10.4P14.2 to the capillary and rotational rheometry data, respectively, (e-f) Flow model fits for E1.93G9.67P17.4 to the capillary and rotational rheometry data, respectively.

the higher prominence of the wall slip behavior with E3.8G10.4P14.2. This is demonstrated through Fig. 4(b) and (c), which show the percent slip and shear contribution values (calculated through Eq. 12) for different nozzles and apparent strain rates corresponding to E3.8G10.4P14.2 and E0G10.2P13.9, respectively. Specifically, each group of three bars corresponds to a different nozzle diameter for low (L), medium (M) and high (H) levels of apparent strain rate levels. Fig. 4 (b) and (c) also demonstrate that the prominence of the wall slip as compared to shear flow increases with decreasing nozzle diameter, a finding that will be further demonstrated in the following sections.

Fig. 4(d-g) presents the results of the flow model fitting to capillary and rotational rheometry data, respectively for two different ink compositions. In Fig. 4(d) and (f), the circles represent data points generated using the relation given in Eq. 4 for various nozzle radii and true wall stress levels within the ranges observed during the experimentation. The curves represent the flow model fits. Each color circle/ curve corresponds to a different stress level, thus considering the experimentally observed wall stress ranges, higher stress data only correspond to larger nozzle sizes. In general, the flow model fits represent the experimental data with decent accuracy as shown. The model parameters for each ink obtained through model fitting are given in Table S2. Results of the statistical analysis of these parameters as a function of compositional variables (Eq. 19) revealed only one statistically significant relationship between the total active material concentration and the flow behavior index n as shown in Table 3 (i.e. stepwise regression process did not include any other parameters in the model thus they are not listed). Accordingly, the flow behavior index reduces with increasing active material concentration, as deduced by the sign of the ρ_{raw} metric for model r_n, indicating more active materials lead to a more prominent shear thinning behavior. This is an expected result since shear thinning in polymer composite suspensions is known to be a product of polymer chain and filler alignment in the flow direction [31].

3.2. Composition-baseline average property relationships

Table 2 lists the average conductivity and porosity for each tested ink composition. The average porosity is in the ~40–50% range and the acetonitrile composition for these inks are in the ~70–75% range, indicating and expected range of 20–30% shrinkage in the printed lines (see Figure S3 for the more detailed porosity data obtained from each experiment). The linear regression results for the models given in Eq 18. obtained using the average conductivity and porosity data is provided in Table 3. As indicated by the sign of the ρ_{raw} metrics for model g*

Table 2
Average conductivity and porosities for all inks.

Ink Composition	Average Conductivity (C^*) (S/m)	Average Porosity (P^*)
E1.8G12.1P13.9	874.2	0.501
E2.9G11.6P14.4	885.0	0.489
E3.8G10.4P14.2	900.9	0.448
E5G10P15	717.4	0.481
E2.6G10.5P17.1	999.0	0.408
E0.5G10.8P17	1230.8	0.458
E1.93G9.67P17.41	1255.8	0.396
E2.9G8.7P17.5	1045.8	0.440
E2G11.2P15.3	864.4	0.478
E0G12P15	954.1	0.529
E0G10.2P13.9	1034.4	0.518

Table 3
Results of the regression analysis for flow behavior index, average conductivity and average porosity.

Term	Coefficient	SSQ	$\rho_{partial}$	*Im*	ρ_{raw}
$n \approx r_n(EG, Gr, PEO, Act)$					
Act	-0.07	0.139	-0.763	6.250	-0.763
Intercept	2.54				
$C^* \approx g^*(EG, Gr, PEO, Act, P^*)$					
P*	-3008.95	140370.20	-0.887	0.000	-0.483
EG	-86.887	158386.00	-0.898	0.007	-0.551
Intercept	2572.30				
$P^* \approx h^*(EG, Gr, PEO, Act)$					
PEO	-0.02	0.011	-0.769	20.226	-0.769
Intercept	0.82				

electrical conductivity decreases with increasing EGaIn concentration and average porosity. For the same model, the numerical values of the SSQ, ρ_{partial} and Im metrics corresponding to the P* and EG are close, indicating approximately equal importance of these variables in conductivity variation. This relationship is visually demonstrated in the 3D plot given in Fig. 5(a). The average porosity is inversely dependent on PEO concentration. Interestingly, the graphene concentration does not seem to have a significant effect on the average ink conductivity.

EGaIn particles at these size scales are known to form insulating contacts with other constituents due to the oxide skin encapsulating the liquid metal [9,10]. It is accordingly expected for these particles to hinder formation of the conductive graphene networks at the high graphene loading levels and cause a reduction in conductivity. Graphene concentration not significantly influencing average conductivity is likely an indication of the tested Graphene concentration range being well above the percolation threshold for this system and not being wide enough to induce a significant conductivity variation. The observed effect of porosity shows that control of porosity becomes an important factor in achieving high conductivity and increasing binder concentration is a way to achieve lower porosity.

3.3. Process-driven conductivity analysis

The analysis results detailing the relationships between the process inputs, intermediate variables and normalized conductivity is given in Table 4. The "black-box" analysis between the process inputs and conductivity (model f) indicates that the conductivity increases with increasing nozzle radius and apparent strain rate, and decreasing with total active material concentration as suggested by signs of the raw correlation metrics (ρ_{raw}) corresponding to these variables. It is seen that the SSQ and Im metrics corresponding to the $\dot{\gamma}_a \times Act$ term is considerably higher than that of the *Act* term alone, suggesting that the active material concentration has its most significant effect through interaction with the apparent strain rate. This leads to the apparent strain rate having most significant effect on the normalized conductivity (also apparent by the magnitude of the ρ_{raw} terms of the three variables). When the relationship between the intermediate variables and normalized conductivity (model g) is observed, one could see that both the slip contribution to the apparent strain rate ($\dot{\gamma}_a^{slip}$)and shear strain rate($\dot{\gamma}$) positively affect the conductivity (as indicated by the positive signs of the corresponding ρ_{raw} terms), with the effect of $\dot{\gamma}$ is being more significant than that of $\dot{\gamma}_a^{slip}$ as indicated by its significantly higher SSQ and ρ_{raw} metrics and approximately equal Im metric between the two variables. Additionally, the effect of the process dependent variation of porosity becomes considerable with increasing shear stress as evidenced by the statistically significant interaction terms between these two variables appearing in the model. Fig. 5(b) shows all the normalized conductivity values for experimental results as a function of $\dot{\gamma}_a^{slip}$ and $\dot{\gamma}$, along with the plane representing by the linear terms associated with these variables in regression function *g*. This 3D plot visually demonstrates the correlation of normalized conductivity with these rate terms. Finally, no correlation between the normalized conductivity and extensional strain rate ($\dot{\varepsilon}$) was observed.

Table 4
Results of the regression analysis for the normalized conductivity.

Term	Coefficient	SSQ	$\rho_{partial}$	*Im*	ρ_{raw}
$\overline{C} \approx f(R, \dot{\gamma}_a, EG, Gr, PEO, Act)$					
R	300000	44200	0.204	0.000	0.167
$\dot{\gamma}_a$	10.231	52438.85	0.221	0.264	0.455
Act	13.567	15564.11	0.123	0.000	-0.056
$\dot{\gamma}_a \times Act$	-0.312	39662.16	-0.193	5.821	
Intercept	-542.040				
$\overline{C} \approx g\left(\dot{\gamma}_a^{slip}, \dot{\gamma}, \overline{P}, EG, Gr, PEO, Act\right)$					
$\dot{\gamma}$	1.982	208188.1	0.419	0.032	0.367
$\dot{\gamma}_a^{slip}$	1.024	142278.4	0.357	0.036	0.323
$\overline{P}$	-23.124	62.107	-0.008	0.000	-0.103
$\dot{\gamma} \times \overline{P}$	-56.325	73359.57	-0.264	0.000	
Intercept	-90.829				

The positive correlation between the shear strain rate and conductivity is rather intuitive. Many studies in the literature demonstrated that one or two-dimensional conductive fillers align during DIW along the shear stresses induced inside the nozzles. In this particular case, increasing shear strain rate likely leads to alignment of the graphene platelets along the printing direction, facilitating the formation of conductive pathways. The SEM image of a sample filament cross-section shown in Fig. 6 highlights a radial alignment pattern within the shear zone where the shear strain rates are non-zero during the flow of a yield-pseudoplastic fluid such as the inks of interest. On the other hand, the positive correlation of conductivity with the slip effects is a non-intuitive observation. Generally, one would expect an increase of slip effects, leading to decrease in shear effects to negatively influence the filler alignment and thus the conductivity in the bulk material. It is possible that the increasing conductivity with the slip effects is associated with the specific wall slip mechanism. It has been reported that one of the prominent wall slip mechanisms during the flow of polymer solutions is the migration of polymer chains from the capillary wall and formation of a low polymer concentration, low viscosity region fluid region, leading significantly high flow velocity gradients near the wall compared to that of the bulk flow [20]. It is possible in this scenario that a similar phenomenon could lead to alignment of graphene flakes under the large strain rates experienced by the solvent rich slip layer near the capillary

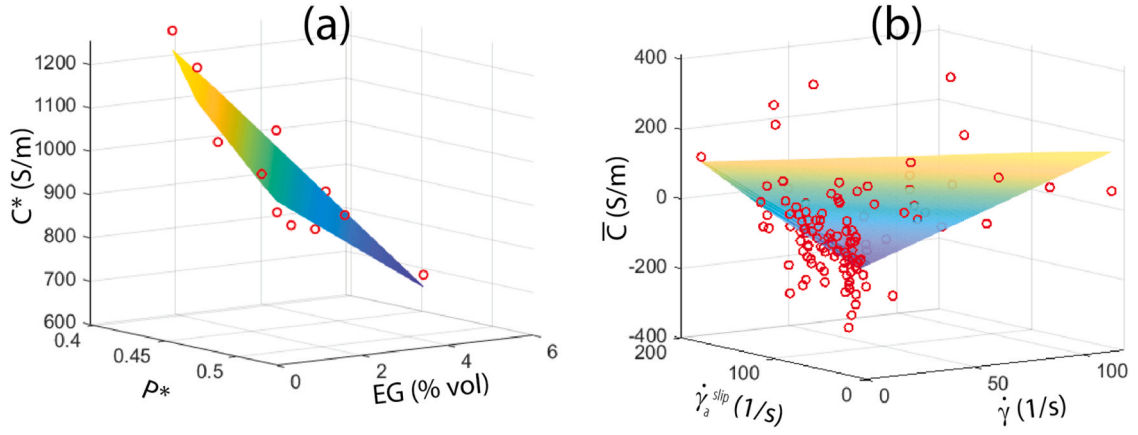

Fig. 5. (a) Average conductivity vs EGaIn concentration and average porosity, (b) Normalized conductivity vs $\dot{\gamma}_a^{slip}$ and $\dot{\gamma}$. 3D views of these figures are provided in the supporting videos.

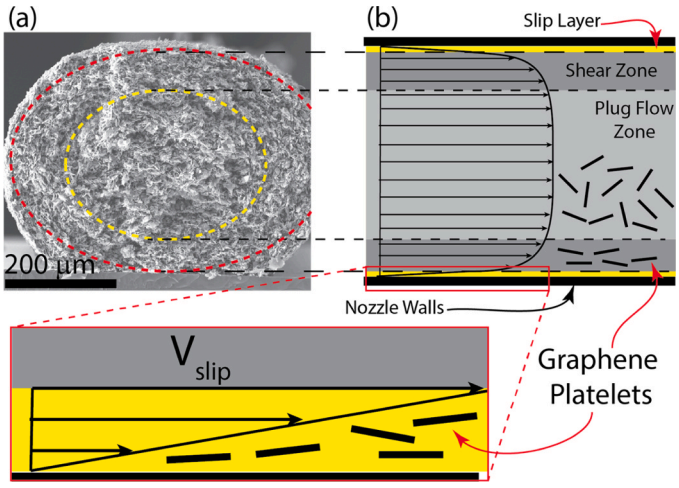

Fig. 6. (a) SEM image of a printed filament cross-section, (b) Schematic representation of a nozzle cross-section, the expected ink flow velocity profile (highlighted by the vectors) and the associated different flow zones.

wall, creating a filament "shell" with high conductivity. The interaction effect between the shear strain rate and the porosity is also expected since the porosity occurs within the core of the filament and its influence on conductivity would only be relevant in cases where the core conductivity is high due to shear alignment of conductive fillers. Finally, it is notable that no ink concentration effects are prevalent in this analysis when the effect of intermediate process variables is considered. Particularly, the effect of the total active material concentration that is observed in the "black-box" analysis is "absorbed" by the intermediate variables, analysis of which is presented below.

3.4. Intermediate variable analysis

Table 5 summarizes the results of the analysis elucidating how the process inputs and ink composition affect the intermediate variables. The ρ_{raw} metrics corresponding to the model $h_{\dot{\gamma}}$ suggest that the shear strain rate is primarily influenced by the apparent strain rate and radius in a positive sense, whereas the total active material and graphene concentration have a negative effect on the shear strain rate. Similarly, $h_{\dot{\gamma}_a^{slip}}$ model parameters indicate that slip contribution increases with decreasing radius, increasing apparent strain rate, graphene concentration and total active material concentration. The influence of the apparent strain rate is observed to be the most important one as it also amplifies the effect of the other variables, as evidenced by the interaction terms that appear in the regression model and the high importance (Im) metric associated with the terms including this variable. Specifically, the apparent strain rate amplified by the graphene and total active material concentration seems to play a significant role in the overall wall slip as the associated Im metric is multiple orders of magnitude higher than the other terms. The model $h_{\bar{P}}$ suggest that the process dependent porosity variation is a pure function of nozzle radius with increasing radius increasing the porosity, as evidenced by the positive coefficient and ρ_{raw} values. Finally, the extensional strain rate estimates do not show any correlation to the input variables.

Table 5
Results of the regression analysis for the intermediate variables.

Term	Coefficient	SSQ	$\rho_{partial}$	Im	ρ_{raw}
$\dot{\gamma} \approx h_{\dot{\gamma}}(R, \dot{\gamma}_a, EG, Gr, PEO, Act)$					
R	113000	6220	0.392	0.000	0.349
$\dot{\gamma}_a$	0.223	8038.845	0.436	0.298	0.398
Act	-2.476	1843.938	-0.226	0.003	-0.133
Gr	-4.854	2696.143	-0.270	0.003	-0.236
Intercept	97.765				
$\dot{\gamma}_a^{slip} \approx h_{\dot{\gamma}_a^{slip}}(R, \dot{\gamma}_a, EG, Gr, PEO, Act)$					
R	-10500	13.1	-0.031	0.0000	-0.170
$\dot{\gamma}_a$	-1.682	779.598	-0.231	0.464	0.910
Act	-1.069	92.240	-0.081	0.000	0.157
Gr	-0.874555	20.61499	-0.03851	0.000	0.008
$R \times \dot{\gamma}_a$	-1246.626	867.7092	-0.24256	0.000	
$Act \times \dot{\gamma}_a$	0.066	1695.479	0.330	21.6	
$Gr \times \dot{\gamma}_a$	0.083	825.483	0.237	2.599	
Intercept	43.336				
$\bar{P} \approx h_{\bar{P}}(R, \dot{\gamma}_a, EG, Gr, PEO, Act)$					
R	169	0.014	0.326	0.000	0.326
Intercept	-0.032				

The significance of the apparent strain rate to the slip contribution is mathematically intuitive. It has also been shown in the literature that the wall slip effects in cylindrical capillaries generally increase with decreasing radius [23,32]. It is also expected for increasing solid content, particularly filler particle concentration to lead to increasing slip effects [33]. It has been shown in Section 3.3 that the regression model between these intermediate variables and normalized conductivity (regression model g in Table 4) does not include any significant compositional variables. Additionally, graphene and total active material concentration both exhibit a negative effect on shear strain rate and positive effect on slip contribution, as indicated by the signs of the corresponding ρ_{raw} metrics corresponding to the model $h_{\dot{\gamma}}$ in Table 5. Thus, relationship of these variables with the two factors determining the process-driven conductivity (shear rate and slip contribution) effectively cancel each other out within the compositional ranges considered, leading them to not appear in model g. It is difficult to reach a definitive conclusion on the influence of EGaIn particle concentration on the intermediate variables using the data available. However, considering that a broader compositional range was examined for EGaIn than that of graphene, one could infer that semi-solid EGaIn particles do not alter the flow mechanisms as much as the more conventional solid fillers.

4. Conclusions

This paper presented an extensive experimental study elucidating the composition-process-property relationships for DIW of graphene-EGaIn-PEO composites. Our results show that the printed structure electrical conductivity is influenced by inherent compositional factors as well as process-driven aspects such as shear flow and wall slip experienced by the inks and the porosity of the printed structures. Regarding the former, interesting conclusions can be drawn from the study where EGaIn particle concentration has a negative effect on conductivity, whereas the polymer binder concentration has a positive effect through reduction of the structure porosity. Analysis of the process related effects showed that in addition to the commonly observed shear flow effects on conductive filler alignment and conductivity improvement, wall slip effects were also found to positively influence the printed structure conductivity. Increasing graphene and total active material concentrations reduced the shear effects while increasing the wall slip effects. These relationships lead to a net negative effect of total active material concentration on process-driven conductivity, which is primarily driven by the ink flow rate and nozzle radius. Specifically, use of larger nozzles led to increased shear and decreased slip effects, resulting in a net positive influence on printed part conductivity.

On ink design, this works presents a "less is more" perspective by revealing that including higher amounts of active materials, even including conductive fillers, may reduce printed part conductivity, through the influence of ink flow mechanisms and porosity. Specifically, regarding the rather uncommon soft EGaIn fillers, one of the key findings of this study is that the inclusion of these fillers in the composites does not contribute to their baseline average conductivity. On the process side, unlike graphene, we have found that EGaIn fillers have a rather neutral effect on shear and slip and thus the associated process-

driven conductivity variation. These findings draw a different picture compared to some of the earlier studies involving different ink compositions and/or EGaIn particle morphologies. Our earlier work on similar material systems [4] with significantly lower graphene loadings showed that EGaIn fillers can have a positive contribution to conductivity. Accordingly, we can conclude that increasing graphene loading reduces the contribution of EGaIn fillers to conductivity, rendering them as conductivity inhibitors. In another recent work, Haake *et al.* demonstrated that EGaIn fillers that are an order of magnitude larger than the ones used in this study, can deform and merge under the shear and extensional flows during DIW, forming conducting pathways [13]. Accordingly, this study demonstrates that such effects are not prevalent for EGaIn particles that are smaller than 5 μm and, in the presence of other rigid fillers.

On process design, the presented results clearly show that higher apparent strain rates lead to high conductivity, most likely due to the shear and slip induced alignment of graphene fillers. This means, at constant nozzle size, higher flow rates and at constant flow rate, lower nozzle sizes are conducive to obtaining higher conductivity. Even though the net isolated effect of increasing nozzle diameter is positive on conductivity, one should note that a statistically significant positive effect of nozzle size on porosity was also observed. Porosity in this context refers to the micro-scale porosity of an individually printed filament. This porosity will adversely affect printed part integrity and strength and thus should be considered during the process design.

Several limitations of the presented study should be noted. First, the limited number of ink compositions tested provide a limited picture of the effect of the compositional parameters. Second, challenges in flow model fitting in the presence of complex wall slip phenomena have been noted in the literature [25]. In this work, the rotational rheology experiments were run at low strain rate ranges due to the known limitations of the method with highly loaded liquids. This leads to high rate behavior of the inks being only characterized by the capillary rheometry. Expanding the compositional space and incorporating additional rheometry techniques such as squeeze flow can alleviate these concerns yet come with a significant experimental cost.

This work should be followed and supplemented by several future efforts to maximize its impact. First, detailed microstructural characterization of printed structures is needed to directly observe the morphology of fillers for various ink compositions and process parameters. Second, the effect of the ink flow outside the nozzles, during the deposition process on the final part properties should be studied. In this study, these effects were isolated through using balanced extrusion and a layer height equal to the nozzle diameters. In practice, lower layer heights and higher flow rates are used, inducing higher strain rates experienced by the inks between the nozzle and the substrate. Finally, as more data is populated using various compositions and processing parameter ranges, emerging data science and machine learning techniques could be utilized to potentially reveal more complex interactions between process inputs and outputs, and realize predictive frameworks for manufacturing parts with as-designed functional properties.

Funding statement

This work was financially supported by the National Science Foundation (NSF) grant 1846758.

CRediT authorship contribution statement

Ruchira Tandel: Writing – review & editing, Writing – original draft, Visualization, Methodology, Investigation, Formal analysis, Data curation, Conceptualization. **B. Arda Gozen:** Writing – review & editing, Writing – original draft, Supervision, Project administration, Methodology, Investigation, Funding acquisition, Formal analysis, Conceptualization. **Irmak Sargin:** Writing – review & editing, Methodology, Formal analysis.

Declaration of Competing Interest

The authors declare that they have no known competing financial interests or personal relationships that could have appeared to influence the work reported in this paper.

Data availability

Data will be made available on request.

Acknowledgements

The authors would like to acknowledge the help of Franceschi Microscopy and Imaging Center at Washington State University for SEM imaging.

Appendix A. Supporting information

Supplementary data associated with this article can be found in the online version at doi:10.1016/j.addma.2024.104101.

References

[1] W. Xu, S. Jambhulkar, D. Ravichandran, Y. Zhu, M. Kakarla, Q. Nian, B. Azeredo, X. Chen, K. Jin, B. Vernon, D.G. Lott, J.L. Cornella, O. Shefi, G. Miquelard-Garnier, Y. Yang, K. Song, 3D printing-enabled nanoparticle alignment: a review of mechanisms and applications, Small 17 (2021) 1–57, https://doi.org/10.1002/smll.202100817.

[2] J.P. Lewicki, J.N. Rodriguez, C. Zhu, M.A. Worsley, A.S. Wu, Y. Kanarska, J. D. Horn, E.B. Duoss, J.M. Ortega, W. Elmer, R. Hensleigh, R.A. Fellini, M.J. King, 3D-printing of meso-structurally ordered carbon fiber/polymer composites with unprecedented orthotropic physical properties, Sci. Rep. 7 (2017) 43401, https://doi.org/10.1038/srep43401.

[3] M.L. Shofner, F.J. Rodríguez-Macías, R. Vaidyanathan, E.V. Barrera, Single wall nanotube and vapor grown carbon fiber reinforced polymers processed by extrusion freeform fabrication, Compos. Part A Appl. Sci. Manuf. 34 (2003) 1207–1217, https://doi.org/10.1016/j.compositesa.2003.07.002.

[4] R. Tandel, B.A. Gozen, Direct-Ink-writing of liquid metal-graphene-based polymer composites: composition-processing-property relationships, J. Mater. Process. Technol. 302 (2022), https://doi.org/10.1016/j.jmatprotec.2021.117470.

[5] S. Nesaei, M.D. Rock, Y. Wang, M. Kessler, A. Gozen, Additive manufacturing with conductive, viscoelastic polymer composites: direct-ink-writing of electrolytic and anodic poly(ethylene oxide) composites, J. Manuf. Sci. Eng. 139 (2017) 1–52, https://doi.org/10.1115/1.4037238.

[6] M. Wei, F. Zhang, W. Wang, P. Alexandridis, C. Zhou, G. Wu, 3D direct writing fabrication of electrodes for electrochemical storage devices, J. Power Sources 354 (2017) 134–147, https://doi.org/10.1016/j.jpowsour.2017.04.042.

[7] M.A. Skylar-Scott, S. Gunasekaran, J.A. Lewis, Laser-assisted direct ink writing of planar and 3D metal architectures, Proc. Natl. Acad. Sci. (2016) 1–6, https://doi.org/10.1073/pnas.1525131113.

[8] B.Y. Ahn, E.B. Duoss, M.J. Motala, X. Guo, S.-I.S.-I. Park, Y. Xiong, J. Yoon, R. G. Nuzzo, J.A. Rogers, J.A. Lewis, Omnidirectional printing of flexible, stretchable, and spanning silver microelectrodes, Science 323 (2009) 1590–1593, https://doi.org/10.1126/science.1168375.

[9] M.G. Mohammed, R. Kramer, All-printed flexible and stretchable electronics, Adv. Mater. (2017) 1604965, https://doi.org/10.1002/adma.201604965.

[10] J.W. Boley, E.L. White, R.K. Kramer, Mechanically sintered gallium-indium nanoparticles, Adv. Mater. 27 (2015) 2355–2360, https://doi.org/10.1002/adma.201404790.

[11] Y. Liu, Q. Wang, S. Bi, W. Zhang, H. Zhou, X. Jiang, Water-processable liquid metal nanoparticles by single-step polymer encapsulation, Nanoscale 12 (2020) 13731–13741, https://doi.org/10.1039/d0nr00988a.

[12] T.R. Lear, S.H. Hyun, J.W. Boley, E.L. White, D.H. Thompson, R.K. Kramer, Liquid metal particle popping: macroscale to nanoscale, Extrem. Mech. Lett. 13 (2017) 126–134, https://doi.org/10.1016/j.eml.2017.02.009.

[13] A. Haake, R. Tutika, G.M. Schloer, M.D. Bartlett, E.J. Markvicka, On-demand programming of liquid metal-composite microstructures through direct ink write 3D printing, Adv. Mater. 34 (2022), https://doi.org/10.1002/adma.202200182.

[14] Y. Sargolzaeiaval, V.P. Ramesh, T.V. Neumann, R. Miles, M.D. Dickey, M.C. Öztürk, High thermal conductivity silicone elastomer doped with graphene nanoplatelets and eutectic gain liquid metal alloy, ECS J. Solid State Sci. Technol. 8 (2019) P357–P362, https://doi.org/10.1149/2.0271906jss.

[15] J. Wang, G. Cai, S. Li, D. Gao, J. Xiong, P.S. Lee, Printable superelastic conductors with extreme stretchability and robust cycling endurance enabled by liquid-metal particles, Adv. Mater. 1706157 (2018) 1706157, https://doi.org/10.1002/adma.201706157.

[16] R. Guo, B. Cui, X. Zhao, M. Duan, X. Sun, R. Zhao, L. Sheng, J. Liu, J. Lu, Cu-EGaIn enabled stretchable e-skin for interactive electronics and CT assistant localization, Mater. Horiz. 7 (2020) 1845–1853, https://doi.org/10.1039/c9mh02066g.

[17] R. Tutika, S.H. Zhou, R.E. Napolitano, M.D. Bartlett, Mechanical and functional tradeoffs in multiphase liquid metal, solid particle soft composites, Adv. Funct. Mater. 28 (2018) 1–13, https://doi.org/10.1002/adfm.201804336.
[18] G. Yun, S.Y. Tang, Q. Zhao, Y. Zhang, H. Lu, D. Yuan, S. Sun, L. Deng, M.D. Dickey, W. Li, Liquid metal composites with anisotropic and unconventional piezoconductivity, Matter 3 (2020) 824–841, https://doi.org/10.1016/j.matt.2020.05.022.
[19] S. Nesaei, D.J. Cavanagh, A. Gozen, Rheology of liquid metal particle-based polymer composites: a comparative study, J. Rheol. 63 (2019) 559–568, https://doi.org/10.1122/1.5082662.
[20] P. Wilms, J. Wieringa, T. Blijdenstein, K. van Malssen, J. Hinrichs, R. Kohlus, On the difficulty of determining the apparent wall slip of highly concentrated suspensions in pressure driven flows: the accuracy of indirect methods and best practice, J. Nonnewton. Fluid Mech. 299 (2022) 104694, https://doi.org/10.1016/j.jnnfm.2021.104694.
[21] P. Wilms, J. Wieringa, T. Blijdenstein, K. van Malssen, R. Kohlus, Quantification of shear viscosity and wall slip velocity of highly concentrated suspensions with non-Newtonian matrices in pressure driven flows, Rheol. Acta 60 (2021) 423–437, https://doi.org/10.1007/s00397-021-01281-5.
[22] T.J. Coogan, D.O. Kazmer, In-line rheological monitoring of fused deposition modeling, J. Rheol. 141 (2019), https://doi.org/10.1122/1.5054648.
[23] K.T. Estelle, B.A. Gozen, Complex ink flow mechanisms in micro-direct-ink-writing and their implications on flow rate control, Addit. Manuf. 59 (2022) 103183, https://doi.org/10.1016/j.addma.2022.103183.
[24] G.M. Eccleston, N.E. Hudson, The use of a capillary rheometer to determine the shear and extensional flow behaviour of nasal spray suspensions, J. Pharm. Pharmacol. 52 (2000) 1223–1232, https://doi.org/10.1211/0022357001777351.
[25] H.S. Tang, D.M. Kalyon, Estimation of the parameters of Herschel-Bulkley fluid under wall slip using a combination of capillary and squeeze flow viscometers, Rheol. Acta 43 (2004) 80–88, https://doi.org/10.1007/s00397-003-0322-y.
[26] Y. Qian, S. Kawashima, Distinguishing dynamic and static yield stress of fresh cement mortars through thixotropy, Cem. Concr. Compos. 86 (2018) 288–296, https://doi.org/10.1016/j.cemconcomp.2017.11.019.
[27] R.H. Byrd, J.C. Gilbert, J. Nocedal, A trust region method based on interior point techniques for nonlinear programming, Math. Program. 89 (2000) 149–185, https://doi.org/10.1007/PL00011391.
[28] F.N. Cogswell, Converging flow of polymer melts in extrusion dies, Polym. Eng. Sci. 12 (1972) 64–73, https://doi.org/10.1002/pen.760120111.
[29] H.B. Harrison, Obtaining specific contact resistance from transmission line model measurements, IEEE Trans. Energy Convers. 4 (1989) 160–165, https://doi.org/10.1109/60.17906.
[30] P.J. Hoffman, The paramorphic representation of clinical judgment, Psychol. Bull. 57 (1960) 116–131, https://doi.org/10.1037/h0045341.
[31] J.C. Majesté, Rheology and Processing of Polymer Nanocomposites: Theory, Practice, and New Challenges, in: Rheology and Processing of Polymer Nanocomposites, 2016: pp. 69–134. ⟨https://doi.org/10.1002/9781118969809.ch3⟩.
[32] P. Deng, J. Zhang, F. Liu, K. Liu, H. Liu, L. Zhang, Shear-induced flow behavior of three polymers in different size dies, J. Macromol. Sci. Phys. 52 (2013) 651–661, https://doi.org/10.1080/00222348.2012.720171.
[33] D.M. Kalyon, Apparent slip and viscoplasticity of concentrated suspensions, J. Rheol. 49 (2005) 621–640, https://doi.org/10.1122/1.1879043.